ISSN: 1231-4005
e-ISSN: 2354-0133
DOI: 10.5604/01.3001.0010.3158

USE OF 3D PRINTING TECHNOLOGY IN THE AVIATION INDUSTRY ON AN EXAMPLE OF NUMERICAL EXPERIMENTAL STRESS STATE ANALYSIS OF UNMANNED AERIAL VEHICLE WING

Łukasz Święch, Arkadiusz Bendarz

Rzeszow University of Technology
Department of Aircrafts and Aircrafts Engine
Powstancow Warszawy Street 8 (L-H30/7), 35-959 Rzeszow, Poland
e-mail: l_swiech@prz.edu.pl abednarz@prz.edu.pl

Abstract

The article presents the results of static tests performed on the primary support structures of a TWISST-ter unmanned aircraft constructed using additive manufacturing techniques commonly known as 3D printing. The primary goal of the experiment was determining the material effort of the structure in order to assess the feasibility of such an engineering solution in terms of material mechanics. Considering the fact that the properties of 3D printed elements are not widely known, both destructive experimental methods and finite element methods were used. During the experimental trails, the ARAMIS deformation measurement system, based on digital three-dimensional image correlation, was used. The results of this experiment allowed for the calibration of the numerical model as achieving convergence with experimentally determined strain fields. This approach ensured the correctness of the numerical determined stress state. Based on the results of the study, the necessary design improvements were implemented and a general conclusion was formed regarding of the numerical analysis of structures made through 3D printing.

Keywords: *DIC, 3d printing, FFF, stress state, UAV*

1. Introduction

A tremendous increase of unmanned aerial vehicles (UAV) interest can be observed. This type of aircraft is finding new applications in aviation such as patrol missions, photogrammetric measurements, and military applications. The simplest designs are made using scale model methods, which use balsa wood or polystyrene as the primary engineering material. More advanced aircraft are built using composite structures reinforced with glass or carbon fibres. Besides the unquestionable advantages of composite materials such as their beneficial strength to weight ratio defined by their specific strengths and the relative simplicity of creating complicated designs, it is worth mentioning the high cost of the material and equipment needed to form it.

The article presents fragments of a study on the application of alternative methods, different from the aforementioned ones, of manufacturing small-unmanned aerial vehicles. Recently, the accelerated progress in the field of these technologies can be especially noticed. There have been advances in both the engineering materials used and the methods used to shape them. The most common methods include fused deposition modelling (FDM) or fused filament fabrication (FFF), and stereo lithography (SL or SLA). Regardless of the version, these technologies allow for the manufacturing of geometrically complex structures at a relatively low cost. As a result, even the production of singular aircraft becomes viable without the need for expensive tooling.

2. FFF Additive Manufacturing

Among the aforementioned methods, the most common spread is fused filament fabrication. The technique was developed in 2005 by Dr. Adrian Bowyer from the University of Bath in Great Britain and distributed as the open source RepRap project.

The available engineering materials include a wide spectrum of polymers like ABS, PC, PET, HIPS, and Nylon, as well as biodegradable materials like PLA, and even composites like ABS-PC or PLA with carbon fibres.

The primary idea of this technology is based on creating objects "layer by layer" [8] by using melted plastic extruded through a nozzle (Fig. 1). Nozzles used in FFF have diameters from as small as 0.2 mm, with some exceeding even 1 mm. The selection of this element determines the dimensional accuracy and builds time of the model [2, 3, 7].

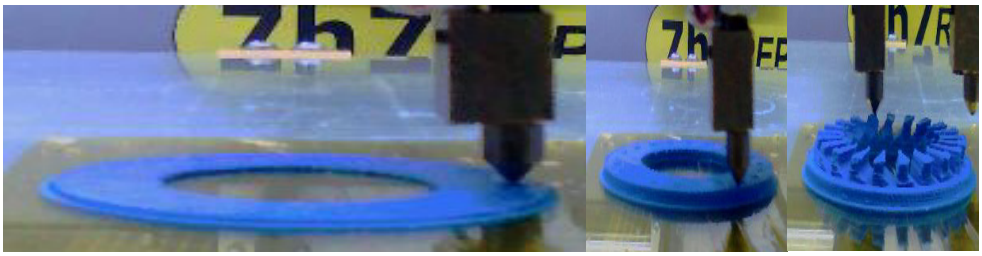

Fig. 1. Example of a model being made with FFF

The mechanical properties of 3D printed objects are dependent on the method of slicing the model; and how it is situated during manufacturing. Fig. 2 presents the results of a tensile test of 3 different types of samples made from ABS (the samples were shaped like the model in Fig. 2). The "A" sample was made in flat position on the print bed and the infill was made of intersecting parallel and perpendicular lines to the length of the model. Sample "B" was printed with an infill with layers rotated 45 degrees from the length of the model. Sample "C", on the other hand, was printed in a vertical direction.

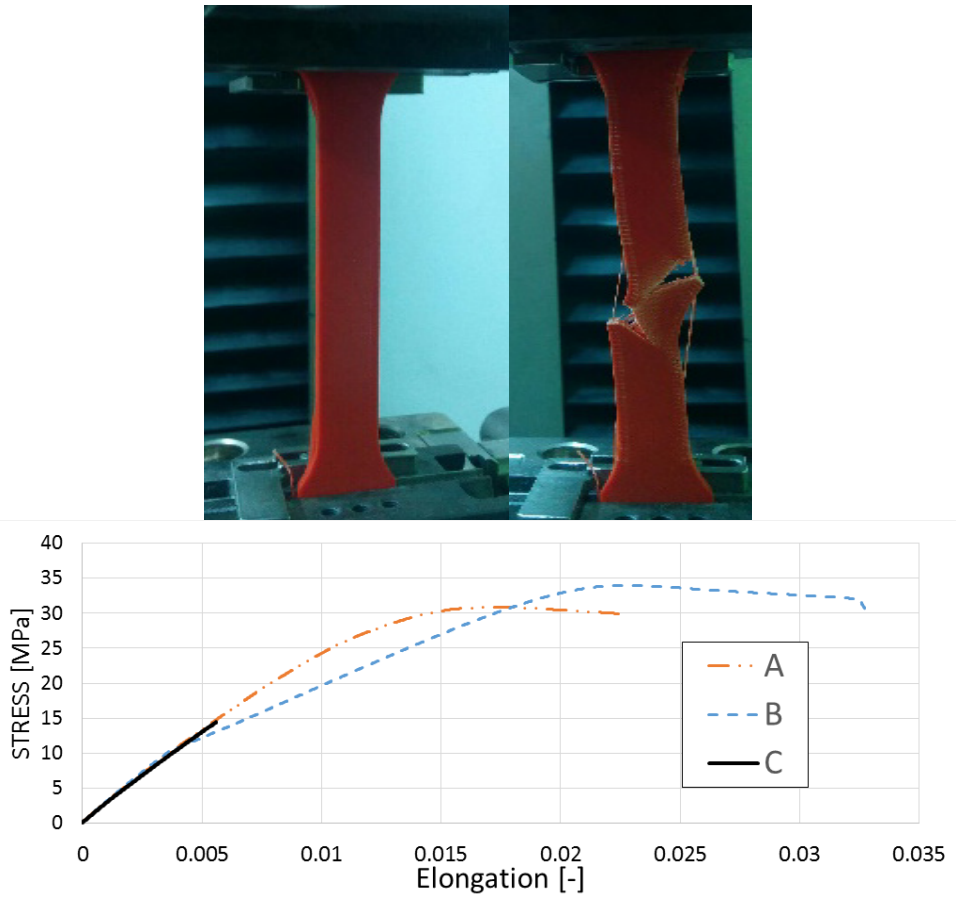

Fig. 2. Tensile test results of samples made from ABS

3. Experiment

3.1. Description of the Tested Vehicle

The experiment consisted of a static test of the centre wing of a TWISST-ter unmanned airplane (Fig. 3). The aircraft features a traditional structure and a wingspan of 2 m, was designed a viability test of manufacturing small aircraft with 3D printing.

The airfoils of the aircraft are completely made using 3D printing with a skin thickness of 0.94 mm. The wing has a cantilever stressed skin design featuring twin spars that are further strengthened [6] by stringers in the front and primary torsion boxes (Fig. 4a). The centre wing is attached to the fuselage through the use of three carbon tubes with a diameter of 5 mm (Fig. 4b).

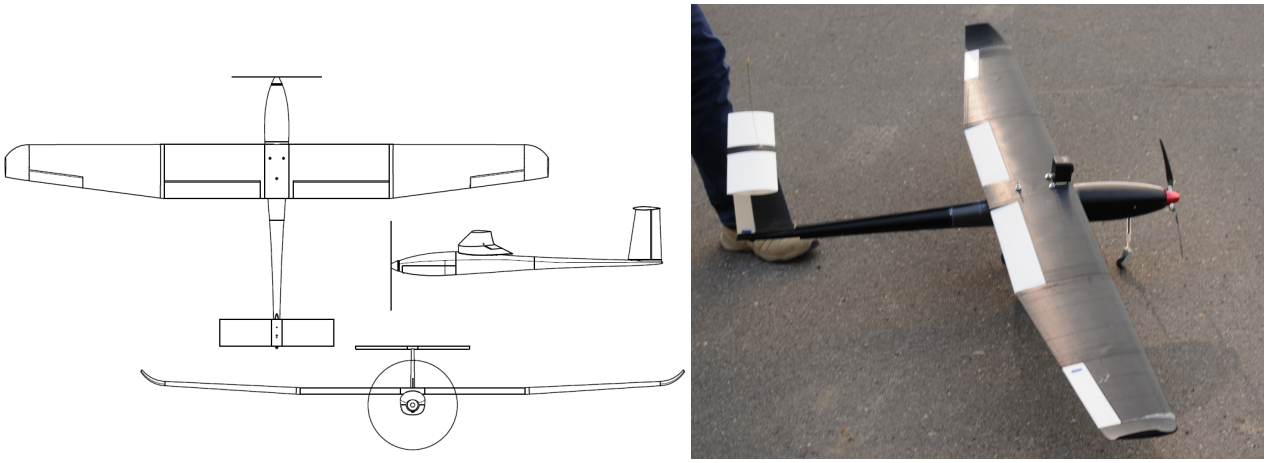

Fig. 3. TWISST-ter unmanned aircraft

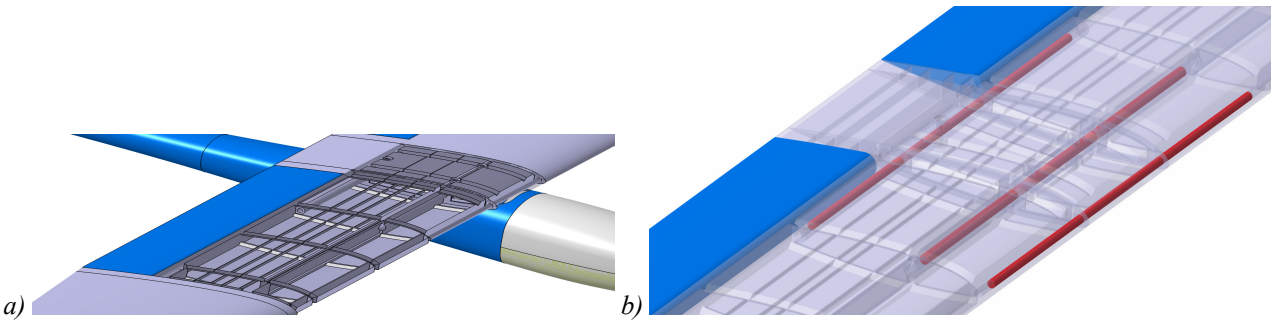

a) *b)*

Fig. 4. Wing Structure of the tested vehicle

3.2. Loads

The primary load applied to the section of the wing consists of the shear force (T), bending moment (Mg) and torsional moment (Ms) that results from the aerodynamic forces that occur because of the flow of air around the airfoil during flight. Fig. 5 presents the distribution of the aforementioned load parameters that result from the calculations of the design stage, which was done in accordance with the Shrenk method [4, 5].

Loading the wing with a distributed load in the form of pressure is problematic when conducting static trails; as a result, a simplified point load is used in practice. During the above-mentioned experiment, a static trail was conducted on the central part of the wing (the segment near the flap) with a normal force working on the mean aerodynamic chord. As a result, this load distribution will demonstrate the effective values of the shear force and bending moment in a sensitive section near the fuselage.

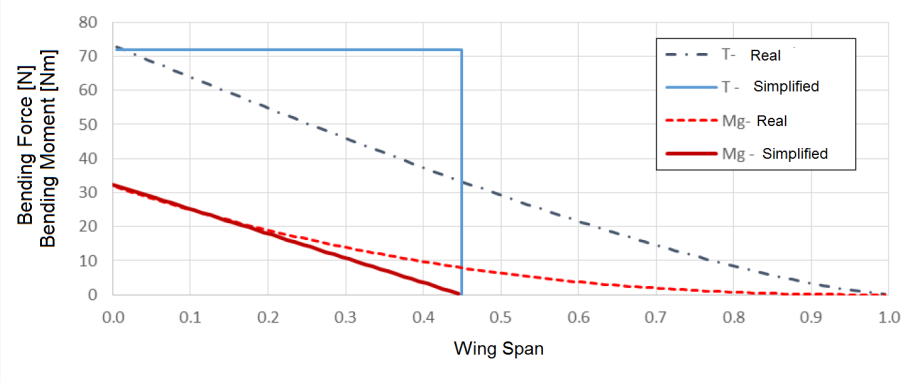

Fig. 5. Load distribution along the wingspan

For the trail, a fragment of the wing was fixed to a wooden base with three screws to simulate the installation of the structure to the fuselage of the aircraft. Loads were applied to the wing surface gravitationally. This guarantees that the force application is independent of wing deflection. The load model and the implementation of test bench are presented in Fig. 6 respectively.

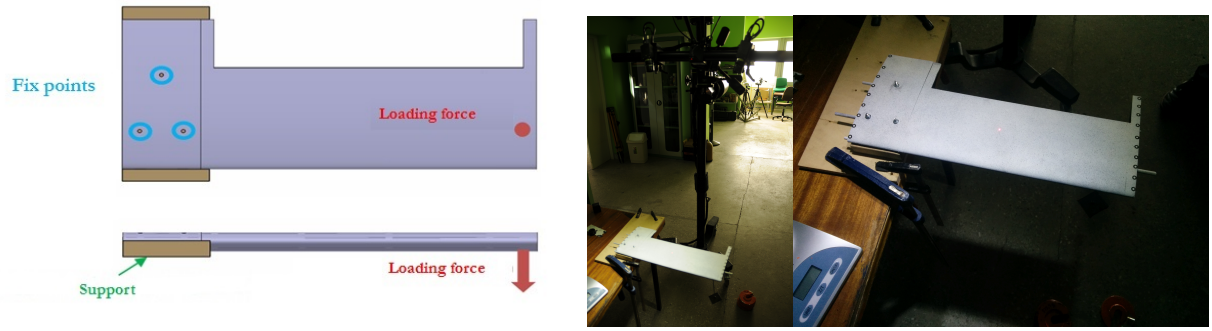

Fig. 6. Wing model and test bench and test bench and loading method

3.3. Deformation Measurement Test – Digital Image Correlation Method

Registering the deformation of the wing surface during the experiment was done with the help of an ARAMIS optical scanner made by GOM mbH, which is based on three-dimensional digital image correlation (DIC).

A numerical − optical method enables three-dimensional measurements of surface deformation regardless of shape [1, 9]. The measurement is based on the digital transformation of the registered image relying on following the changes in pixel distribution in the photographs. The device is comprised of two digital cameras connected to a PC together making the measurement system.

Before the trail, a calibration of device was conducted to define the measurement area. A measurement area of 450x450 mm was selected for the needs of the experiment. The measurement is done by taking a series of photographs of the prepared test subject during its loading. Preparing the test subject is done by covering the surface with white paint that is then covered with a stochastic pattern of black spots.

The system divides photographs of the surface of the test subject into a series of subsections. As a result, the system creates a strain mesh (Fig. 7). Each element of the mesh has a unique pattern of spots in its vicinity, which is the basis for identifying its location in the established coordinate system. Both of the cameras' images are compared in order to introduce a third dimension. The first set of images is considered to the reference state. Surface strain on the test subject causes a change in distribution of spots in each mesh element. After comparing the positions of the spots to the initial

reference state, the displacement of the spots is calculated. The precision of the measurement is dependent on the accuracy of the calibration procedure, potential errors during matching images during image correlation procedures (image errors), as well as the quality of the applied spot pattern. Eventually, the accuracy of the displacement measurement is between 1 μm to 5 μm.

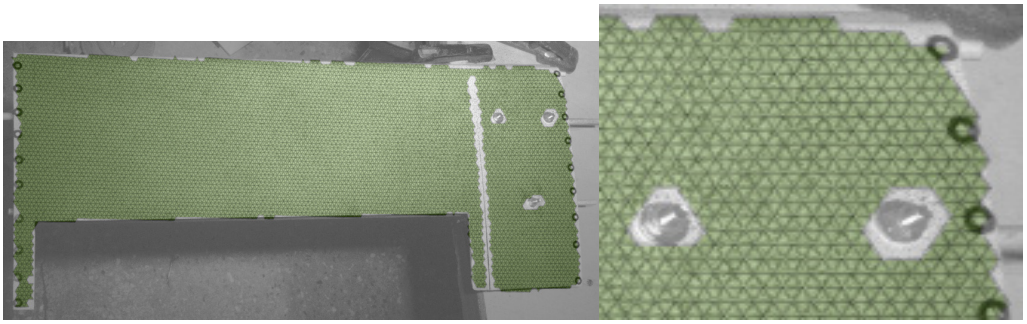

Fig. 7. Wing surface with strain mesh division

As a result, the measurements provide quantitative data on the scale of the displacement of the recorded surface area during the experiment (Fig. 8). The results are presented as a visualization using colours to represent FEA results, allowing for the comparison of individual results.

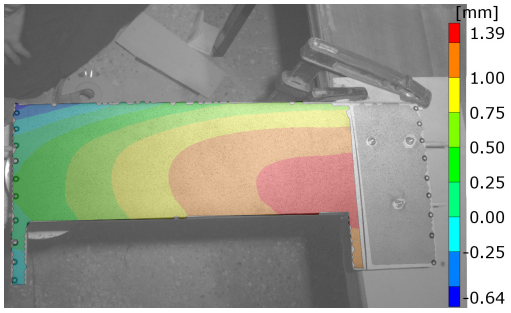

Fig. 8. Example of ARAMIS system measurement result – displacement along the wingspan

4. Numerical Analysis

4.1. Numerical Model

The wing model that was initially prepared for 3D printing was imported into the Ansys Workbench 17.0 program and modified for numerical analysis. Fig. 9 presents the appearance of the model. Based on the geometric model of the centre wing, a series of discrete model contain various numbers of finite elements and force values applied to the system. An optimized number of finite elements used in the analysis were established during the early stages of the study. The model was constructed using TET-10 elements, which have a quadratic shape function (Fig. 9).

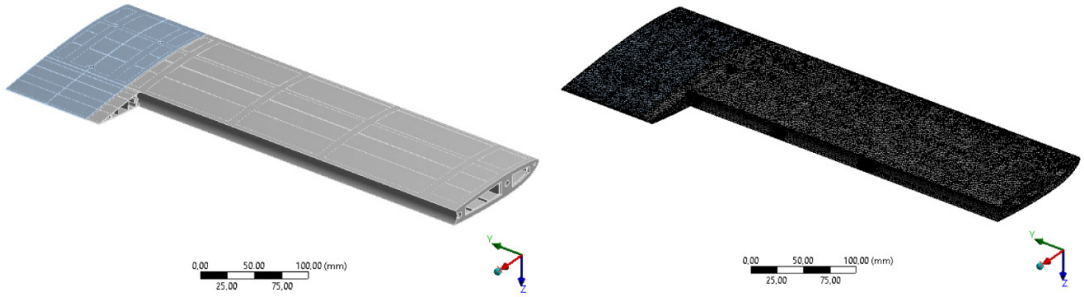

Fig. 9. Wing numerical model used in numerical analysis and discrete model comprised of over 169000 TET-10 elements

4.2. Analysis Preparations

The material models used in the analysis preparations were defined as being linearly elastic. Constant values for the materials, critical for calculation, based on experimental data are presented in Tab. 1. Thermal effects were ignored in the analysis.

Tab. 1. Material constants

Material name	Elements	Young's Modulus	Poisson Ratio
		MPa	-
ABS	Wing, connector	1300	0.35
Carbon	Wing supporting tubes	45000	0.29

The configuration was loaded by a hexagonal element placed at the intersection point of the rib and main spar of the wing. A force of 85 N reflected the experimental loading conditions. The contact points between the support surfaces and carbon tubes were identified as frictional w a coefficient of friction of 0.15. Such contact points permit replicating the actual changes in the experimental model (the movement of the carbon tubes out of the wings). Removing all of the degrees of freedom in the connector was the last step of preparing the analysis.

4.2. Wing Deflection

The main source of information regarding the data convergence from the numerical and experimental analysis is the wing deflection during the trail and the type of deformation. This comparison is presented in chapter 5. The maximum displacement in the Z-axis is located at the end of the wing, for a load of 85 N; the wing displacement is higher than 61 mm. The main factor affecting maximum displacement is the Young's modulus of material. It can also be observed that a split appears between the connector and wing. It results from the movement of the carbon tubes out of the wing.

4.3. Stress Distribution

The distribution of maximum reduced stresses facilitates determining the sensitive points of the proposed design. Assuming that the similarity of displacement from different studies will correspond to similarity in stress. It is possible to determine the stress in the wing.

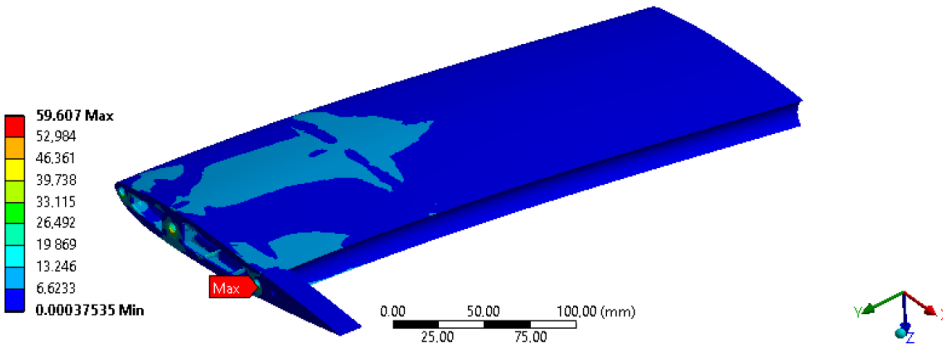

Fig. 10. Reduced stress distribution MPa on the wing surface

The greatest material effort can be observed in the areas of contact between the wing and carbon tubes. This is due to pressure that appears during the bending of the structure, which results from the difference in stiffness of the two pieces. The maximum reduced stress is about 59 MPa (Fig. 10 and Fig. 11). Interpreting this information can be used to make necessary changes to the geometry of the wing in this place. Across the entire image, the locations of the internal ribs are clearly visible.

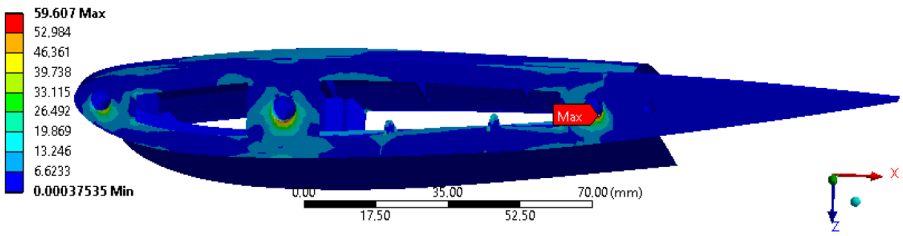

Fig. 11. Reduced stress distribution MPa near the wing mounting points

Similar conclusions can be made about the maximum reduced stresses for connector. The maximum value is nearly 70 MPa, which is representative of the area where the carbon tubes connect both parts of the structure.

The resulting maximum reduced stresses within the wing are a local effect related to the contact between the wing and the tubes (the tube has perfectly sharp edges in the analysis while in reality they have a fillet).

3. Results comparison

The most important measurement affecting the evaluation of both analyses is the displacement distribution (wing deflection). During the experiment analysis, the maximum wing deflection was 66.85 mm when loaded with 85 N (Fig. 12). During numerical analysis, the maximum displacement was 61.33 mm in the Z-axis (Fig. 12). The shapes of displacement of both models are similar. Primarily, the difference between the two analyses is accuracy of fixing the actual model during the experimental trails. During the trails, it was noticed that the connector lifted (rotation around the contact line between the connector and the wing). This was caused by the method of connecting the wing to the test bench. A minimal rotation of the connector caused a rotation of the entire structure and as a result an increase in wing deflection. Additionally, numerical model was shorter about 20 mm.

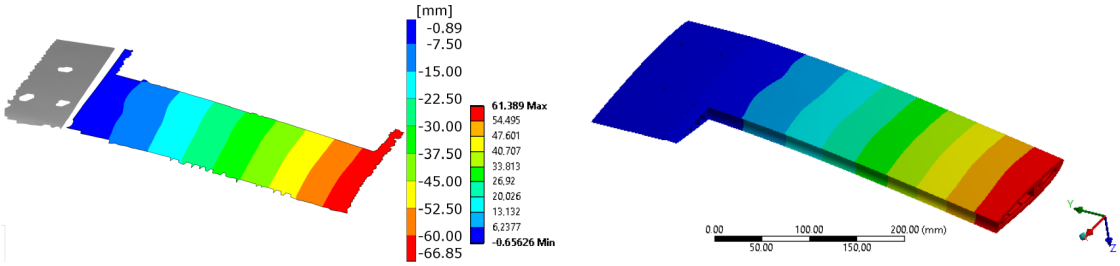

Fig. 12. Experimental method wing surface deflection – 85 N load and numerical method wing surface deflection, mm – 85 N load

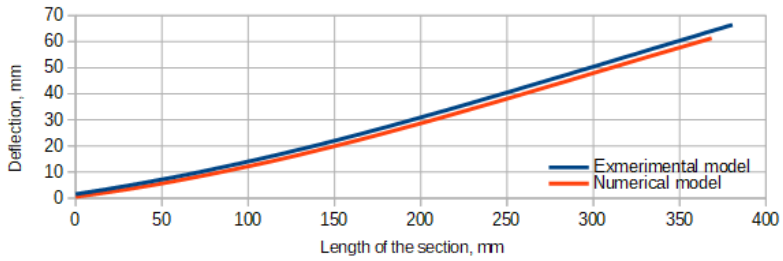

Fig. 13. Wing deflection along the section of the main spar – 85 N load

In the numerical analysis case, there was no assumption used for an ideal fixture of the connector. There was no rotation of this part, thus the results should be lower. The difference between the results can be observed in Fig. 13, which presents the wing deflection distribution along the wingspan. Based on the aforementioned, it can be stated that the results are convergent.

The differences can be accounted for by the attachment of the wing during the experimental trails and the inaccuracy of the FEA boundary conditions. Additionally, both models behaved similarly; and were not destroyed, which shows that the experiment was conducted correctly.

4. Conclusion

The result convergence of the numerical and experimental analyses provides support that FEM model was made correctly. Considering the fact that the study was conducted in the elastic range of the material, which has a linear relationship between the strain and strain. Also, this supports the correctness of the results attained from the numerical material effort distributions.

Below, the sensitive areas of the design are presented where the stress is most highly concentrated. It can be noted that the local peak stress of up 59 MPa appear in one place (tensile strength of the ABS material is about 40 MPa), where the solid is simple. This can be identified as a geometric model error. As a result, this value can be considered as a numerical error caused by an incorrectly prepared model.

It should be noted, that the level load used during the experiment coincides with the flight of the aircraft with an overload coefficient of approximately 7. This value can be observed in highly turbulent atmosphere and during complex acrobatic manoeuvres. In the case of small-unmanned aircraft used in patrol missions, these situations are highly unlikely; a realistic overload coefficient would not exceed 4. It should be acknowledged that the analysed structure satisfactorily meets the conditions of safe operation.

The sufficient static strength, demonstrated during the tests, does not exhaust the research potential because during the operation, the support structures of the aircraft are subjected to time-varying loads. Therefore, it is advisable to determine, through experiments, the fatigue of structures produced using 3D printing.

Acknowledgements

Results presented in this article were obtain by works carried out under the project LIDER / 011/443 / L-4/12 / NCBR / 2013 dated 01.10.2013 funded by The National Centre for Research and Development in Warsaw, under the LIDER IV competition.

References

[1] *ARAMIS: User manual*, GOM mbH, 2010.
[2] Furyk-Grabowska, K., Wyszyński, D., *Analysis of the selected problems of 3D printing using the FFF method*, Stal Metale & Nowe Technologie, 9-10, pp.128-131, 2016.
[3] Łyżwa, A., *Ways to increasing performance of FFF 3D printing method*, Mechanik, 12, pp.1900-1901, 2016.
[4] Schrenk, O., *A simple approximation method for obtaining the spanwise lift distribution*, NACA TM 948, 1940.
[5] Skarbiński, A., Stafiej, W., *Projektowanie i konstrukcja szybowców*, WKŁ, 1965.
[6] Stava, O., Vanek, J., Benes, B., Carr, N., Mech, R., *Stress Relief – Improving Structural Strength of 3D Printable Objects,* 2012.
[7] Szmidt, A., Rębosz-Kurdek, A., *New approaches of improving FDM/FFF printing techology*, Mechanik, 3, pp. 258-261, 2017.
[8] Vaezi, M., Chua, C. K., *Effects of layer thickness and binder saturation level parameters on 3d printing process*, The International Journal of Advanced Manufacturing Technology, Vol. 53, Iss. 1, pp 275-284, 2011.
[9] Zafar, A., *Digital image correlation*, CEE 498KUC – Experimental methods in Structures and Materials, 2008.